Materials Advances

ROYAL SOCIETY OF CHEMISTRY

REVIEW

View Article Online
View Journal | View Issue

Cite this: *Mater. Adv.*, 2022, 3, 3041

Materials prepared by Freezing-Induced Self-Assembly of Dispersed Solutes: A Review

Ranajit Mondal and Guruswamy Kumaraswamy *

Received 1st November 2021,
Accepted 11th February 2022

DOI: 10.1039/d1ma01017d

rsc.li/materials-advances

Crystallization demands structural regularity. Therefore, when a solvent is frozen to form a crystalline solid, it forces the dispersed solute to partition out of the crystalline phase. This forms the basis of ice-templating, wherein a solvent (often water) containing dispersed particles and/or macromolecules is frozen so that the dispersed solute phase is expelled by the ice crystals and is consolidated at their boundaries, when the ice crystals impinge. Removal of the ice crystals results in the formation of a macroporous material, whose pores are bounded by walls formed by the freezing-induced self-assembly of the solute. This versatile technique can be applied to a wide variety of solutes since their expulsion and aggregation due to solvent freezing is largely independent of solute chemistry. Ice-templating has therefore become an increasingly popular synthetic tool in the materials science community. In this review, we summarize the process of freezing and the interaction of the solute with the freezing solvent. We specifically review the literature on how solute–solute interactions influence the self-assembled structure that results from ice templating, and identify lacunae in our current understanding of ice-templated materials synthesis.

1 Introduction

Self-assembly has been defined as the "autonomous organization of components into patterns or structures without human intervention".[1] Self-assembly provides an attractive route to the synthesis of materials with engineered structures and has emerged as an exciting frontier area of research. For materials comprising colloidal or macromolecular building blocks, or for composites comprising inorganic nanoparticles and organic macromolecules, several self-assembly schemes have been explored in the literature. For example, spherical particles with a monodisperse size distribution have been crystallized into three-dimensional periodic structures with precise thickness using convective deposition[2] that balances interparticle interactions, capillary forces and gravitational drainage. Similarly, particle and composite films have been formed using dip coating.[3,4] Electrodeposition[5] where particle deposition is controlled by external electric fields, assembly at fluid–fluid interfaces,[6,7] dewetting,[8] evaporation[9] and polymerization-induced self-assembly of polymers with varied architectures (linear, star-like, bottlebrush-like, *etc.*)[10,11] have emerged as simple yet powerful protocols to prepare materials with control over self-assembled structures. Self-assembly around sacrificial porogen templates has been used to prepare porous materials.[12–15] Among the most industrially important examples of such materials are crystalline microporous zeolites[16] and mesoporous materials with ordered pores.[17] Such materials are not the focus of this review. Porogens have also been used to prepare macroporous materials, such as foams, where chemical blowing agents are used to create gas bubbles as porogens.[18] In aerogels[19] and zerogels, a porous structure results from covalent coupling (typically of oxides). Porous materials have also been obtained by templating a variety of static[20–26] and dynamic[27–33] structures. In particular, there has been a revival in interest in the use of ice as a template to prepare macroporous materials using ice-templating or ice-segregation induced self-assembly. The process of self-assembly in such materials is the focus of this review. The use of water as a porogen makes ice-templating an environmentally benign strategy for material synthesis. In recent years, there has been extensive investigation of the mechanism of ice templating, leading to a deeper understanding of the methods to control structure formation using this process. This has resulted in the use of ice templating to create well controlled self-assembled structures such as colloidal chains,[34,35] 2D colloidal sheets,[36] fibers, membranes,[37–39] core–shell fibers,[40] flakes,[41] porous micro-spheres,[42] and 3D porous monoliths based on ceramics,[43–45] polymers,[46] biomacromolecules,[47–50] metals[51–53] and carbon based materials.[54–59]

Functional materials with remarkable properties have been prepared using ice-templating. For example, biomimetic layered structures inspired by nacre, with brittle inorganic

Soft Materials for Sustainability, Department of Chemical Engineering, Indian Institute of Technology Bombay, Mumbai-400076, India.
E-mail: guruswamy@iitb.ac.in

sheets separated by dissipative layers, have been reported. Such composite materials exhibit outstanding mechanical properties despite a high loading of the brittle inorganic phase, such as a combination of rigidity and toughness.[60–63] Control over the state of solvation of the macromolecular phase in ice-templated polymer–inorganic composites has been exploited to produce macroporous sponges capable of recovering from large compressive deformation.[64] Such exquisite control over hierarchical structuring and over the mechanical properties of ice-templated assemblies has been exploited to prepare materials with relevance to diverse technological areas ranging from biomedical implants, energy storage, and electronics to aerospace. For example, inorganic sponges with an unprecedented combination of viscoelastic shape memory and fire retardancy (obtained without the use of environmentally hazardous flame retardant additives) have been reported,[65] as have next generation electrode materials[66] for lithium ion batteries tolerant of the volume phase-transitions experienced during electrochemical reactions.[67–70] The growing technological importance of ice templated materials has been documented in several recent reviews that focus on several different aspects of structural control or technological relevance in specific areas.[71–78]

The basic premise of preparing materials using ice-templating appears deceptively straightforward. An aqueous dispersion of solute (here, we use the term solute to refer to dissolved macromolecules as well as dispersed colloidal particles) is frozen. Ice crystals nucleate and grow, expelling the solute to the liquid regions. When the ice crystals impinge, the solute is consolidated at their boundaries. At solute volume fractions of a few percent, a three-dimensionally percolated structure results, with walls comprising the self-assembled solute. If the solute in the walls is held together subsequent to the removal of the ice, then a self-standing macroporous monolith results, with the pore size and shape corresponding to those of the template ice crystals. However, this apparent simplicity masks significant complexity associated with the physics of freezing, the nature of the solid–liquid interface and the influence of the solute on this process. Freezing is associated with the evolution of latent heat, setting up a thermal gradient at the freezing interface. Furthermore, depending on the interaction of the solute with the freezing front, it can either be expelled at the boundary or the ice can grow around it, engulfing the solute particle. This can result in the setting up of a solute concentration gradient at the freezing interface. While most treatments of ice templating deal with the case of dilute solute interacting with a freezing front, in practical situations, one is confronted with phenomena that arise from solute–solute interactions, especially when the solute concentration increases as the ice-templating progresses. Understanding these processes in detail is important to achieve structural control over the self-assembled materials resulting from ice templating. In this review, we provide an overview of these critical aspects of ice-templating. In the next section, we discuss the process of freezing and the nature of the frozen interface. Then, we discuss the interaction of the solute with the freezing front. Finally, we provide a perspective of the influence of solute–solute interactions on the development of ice-templated structures and outline a few aspects that remain incompletely understood. Previous reviews have not specifically concentrated on the aspect of the control of solute–solute interactions as a means to influence the structure of ice-templated materials. We hope that this review provokes investigations into this aspect of ice templating.

2 Freezing

Freezing-induced material preparation has been performed using a variety of solvents apart from water, including camphene, terpene, tertiary butyl alcohol, *etc.* Several aspects of freezing-induced solute consolidation are similar for water and other solvents. For simplicity, we refer to freezing-induced self-assembly as ice-templating in this review, since most reports investigate the freezing of aqueous dispersions. Freezing of water to form ice is a first order phase transition, and is associated with a discontinuous change in the first derivative of free energy (such as the specific volume) and in molecular packing, from a phase with liquid-like order to one with crystalline symmetry. This phase transition occurs through a nucleation and growth process, in which a crystalline phase nucleus with a critical size needs to form before the phase transition can proceed. Under typical laboratory experimental conditions of atmospheric pressure, water crystallizes below 0 °C into the hexagonal form of ice, which has a density of $\approx$920 kg m^{-3}, lower than that of liquid water. For ice crystals to nucleate, water needs to be supercooled below the equilibrium melting point. With an increase in the degree of supercooling, there is an increase in the nucleation density. However, it is to be noted that the nucleation of ice depends not only on the degree of supercooling, but also on the presence of heterogenous surfaces that enhance epitaxial nucleation and, on impurities that could either enhance or inhibit nucleation.[80] Therefore, while it is already challenging to predict crystal nucleation rates in well-defined model systems,[81] it is currently impossible to predict ice crystal nucleation densities in experimental samples. After the formation of a critical nucleus, water molecules rapidly add to the ice crystal as it grows. This addition results in the release of latent heat. For the growth of the ice crystal, water molecules need to diffuse into the growing crystal front and the liberated latent heat needs to be removed. Water is characterized by a thermal diffusivity ($=k/\rho C_p$, where k, ρ and C_p are the thermal conductivity, density and specific heat at constant pressure) of $\approx$0.14 mm^2 s^{-1} at 25 °C. Since freezing is typically effected by cooling a liquid sample in a container, uniform cooling to ensure uniform sized ice crystals necessitates that the sample be thin (*viz.* the sample dimension, $L \ll \left(\frac{kt_I}{\rho C_p}\right)^{0.5}$, where t_I is the induction time for ice nucleation). For larger samples, temperature gradients result, leading to a spatial variation in the nucleation density and size of ice crystals and/or growth of oriented ice crystals. One strategy that has been reported[65] to produce uniform size ice

crystals in large samples is to induce convective flows so that temperature variations are minimized. Often, samples are frozen by intentionally imposing a temperature gradient[82,83] so as to force the directional growth of ice crystals, resulting in the formation of anisotropic, oriented pores in the resultant self-assembled material. Unidirectional propagation of a crystal front is described by the classical Stefan problem that assumes diffusive heat transfer of the latent heat released for one dimensional propagation of a planar freezing front. However, the planar front is unstable and forms lamellar fingers due to the presence of a solute, as will be described in the next section. Lamellar ice crystals do not grow exactly along the temperature gradient direction, but at an angle to it and exhibit a dendritic shape. This has implications for the porous materials that result from ice-templating unidirectionally frozen samples. The imposition of a unidirectional temperature gradient results in the formation of multi-domain lamellar structures, *viz.* the global alignment of lamellae in the sample is not uniform. Researchers have shown[84] that the samples subjected to bidirectional freezing (*viz.* with temperature gradients in two orthogonal directions) show lamellar morphologies that are aligned over the sample size. In addition, researchers have also explored the consequences of radial freezing[85] and freezing under flow,[61] to control the microstructures of ice-templated materials.

It is now accepted that there is a thin layer of quasi-liquid water at the surface of ice. Recent simulations suggest that this layer is characterized by a higher density than bulk water.[86] The presence of this mobile layer at the ice interface has important implications for facilitating reactions at the ice surface, and therefore, for materials synthesis during ice templating. While the structure of this layer has attracted attention in the literature,[87–90] the relevance of this to ice templating has not been considered. Freezing of water containing dissolved salts results in charge separation and trapping of ions in ice, giving rise to an electrostatic potential at the ice surface. This influences the interaction of the freezing front with solutes and could influence solute self-assembly during ice templating.

3 Interaction of the solute with the freezing front

The presence of a dissolved solute leads to a concentration-dependent decrease in the freezing point of the solvent. Since the solute is substantially excluded from the frozen solvent, there is an increase in the solute concentration over a layer of thickness Δ at the freezing front, where $\Delta = D/v$ is the ratio of the solute diffusivity D to the velocity of the growing front v. This increased solute concentration decreases the equilibrium liquidus temperature over Δ, leading to a constitutive supercooling, recognized by Rutter and Chalmers[91] and by Keith and Padden.[92] Thus, the growth velocity of the freezing front is determined not only by diffusion of latent heat, but also by solute-induced constitutive supercooling. This renders the freezing front unstable to perturbations, a situation that was first analysed by the celebrated paper of Mullins and Sekerka.[93] They performed a linear stability analysis of a planar freezing front, assuming purely diffusive flux of the solute at the interface and obtained an analytical expression for the growth of perturbations of the freezing front. Despite the severe simplifications inherent in their analysis, this model provides a good estimate of the lamellar periodicity observed during unidirectional freezing. Dispersed colloidal particles also lead to constitutive supercooling at the freezing front[94] and decrease the melting point of the solvent T_f as,

$$T_f = T_m\left(1 - \frac{\Pi(\phi)}{\rho_l L_f}\right) \quad (1)$$

where T_m is the melting point of pure solvent, $\Pi(\phi)$ is the osmotic pressure at a colloidal volume fraction ϕ; ρ_l and L_f are the solvent density and latent heat, respectively. Thus, the freezing point of a colloidal suspension is a function of the concentration and size of the colloids, and the cellulation of a planar freezing front is a function of the particle concentration, the inter-particle interactions that determine $\Pi(\phi)$, and the front velocity. During freezing of a colloidal dispersion, particle rejection at the freezing front is energetically favourable when the change in the interfacial free energy is positive, *viz.*,

$$\Delta\sigma = \sigma_{ps} - (\sigma_{pl} + \sigma_{sl}) > 0 \quad (2)$$

where σ_{ps}, σ_{pl} and σ_{sl} are, respectively, the particle/solid(ice), particle/liquid and solid(ice)/liquid interfacial free energies. This energy criterion can be used to analyse systems where dispersed isolated colloidal particles experience both attractive (F_A) and repulsive (F_R) forces at the growing interface, given as,

$$F_A = \frac{6\pi\eta v R^2}{d} \quad (3)$$

$$F_R = 2\pi R\Delta\sigma\left(\frac{\alpha_0}{d}\right)^n \quad (4)$$

where η is the fluid viscosity, R is the radius of the colloidal particle, v is the velocity of the growing ice front, d is the thickness of the liquid film between the particle and the interface, α_0 is the mean distance between the liquid molecules and n is an empirical correction factor that generally ranges from 1 to 4, depending on the particle dimensions and the system. The balance of these two forces in the absence of gravity gives the critical velocity as,

$$v_c = \frac{\Delta\sigma d}{3\eta R}\left(\frac{\alpha_0}{d}\right)^n \quad (5)$$

Below v_c, the particle is rejected at the freezing front while for growth velocities that exceed v_c, the particle is engulfed as the frozen phase grows around it. This represents a somewhat simplified picture of the interactions between a particle and a freezing front. A more complete picture needs to explicitly consider a variety of interactions depicted schematically in Fig. 1. Deville has recently reported[95] experiments where a growing planar freezing front encounters monodisperse oil droplets of different sizes. They show that isolated droplets

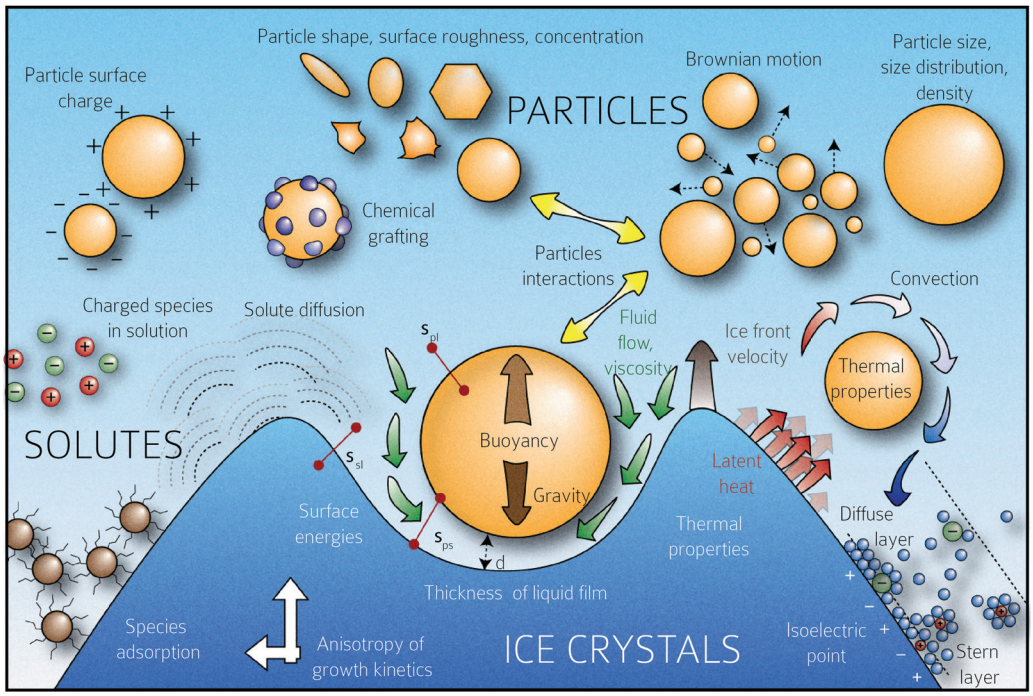

Fig. 1 Schematic representation of the multiplicity of interactions between the freezing front and solutes (particles, polymers, charged species, *etc.*) The rich physics inherent in this situation, from growth instabilities of the growth front, hydrodynamic interactions between the front and solute, charging and electrostatic interactions between the species, solute–solute interactions, and species diffusion, among others, are schematically depicted. Copyright (2016) Sylvain Deville (DOI: 10.6084/m9.figshare.4012677) CC BY 4.0 https://doi.org/10.6084/m9.figshare.4012677.v1.

are rejected at the freezing front when they are smaller than a critical size while larger droplets are engulfed. However, when multiple small droplets are accumulated at the freezing front, they interact to form larger droplet clusters that are engulfed by the freezing front. Omenyi *et al.* identified an inversely proportional relationship between the critical solid/liquid interface velocity and particle size[79] for naphthalene/nylon-6,10 and biphenyl/nylon-l2 systems as illustrated in Fig. 2. There is a critical velocity of the growing solidification front above which particles become entrapped for a given particle size. Particles are rejected at the front, only for growth below this threshold velocity. Inversely, there is a critical particle size for entrapment for a given displacement velocity: particles larger than the critical size are entrapped, whereas smaller ones are repelled. Deville *et al.* have also elucidated a general stability analysis for the solidification of colloidal suspensions over a range of interface velocities and particle sizes.[96] Their observation revealed that small colloidal particles (of the order of microns or smaller) are rejected when they encounter a freezing front propagating at low interface velocity (<1 μm s^{-1}). Here, the liquid freezes such that the interface proceeds as the planar front and the colloids are rejected and are concentrated in the unfrozen region. As the front velocity exceeds a critical value, it is destabilized to form lamellar structures due to constitutive supercooling, as described by Mullins and Sekerka.[93] On further increasing to still higher interface velocities (>1 mm s^{-1}) the morphology of the interface remains planar but the colloidal particles are engulfed by the growing front and show no spatial redistribution. Interesting porous morphologies where solute particles self-assemble into walls result at intermediate velocities of the freezing front (1 μm s^{-1} –1 mm s^{-1}) and for intermediate solute particle sizes. Here, the particles are excluded as the solvent crystallizes and are consolidated between the growing lamellar crystals.

4 Solute–solute interactions for control of self-assembled structures during freezing

As seen in the previous section, the interaction of a dispersed colloidal particle with a freezing front has been studied in depth. Often, such studies have been performed for unidirectional propagation of a freezing front, driven by a temperature gradient. If the dispersed phase colloidal particles are sufficiently small that they are Brownian, then under a wide range of practically realizable freezing conditions, they are expelled at the freezing front. Thus, their concentration in the dispersed phase increases until the ice crystals impinge after completion of freezing. The structure of the final assembly is determined by inter-particle interactions as well as by geometrical aspects of the consolidation of dispersed colloidal particles by growing ice crystals. Here, we explore the literature on how these aspects determine the structure of the assemblies. The mode of freezing the sample (uniform cooling *versus* unidirectional propagation of a freezing front) influences the geometry of ice crystal

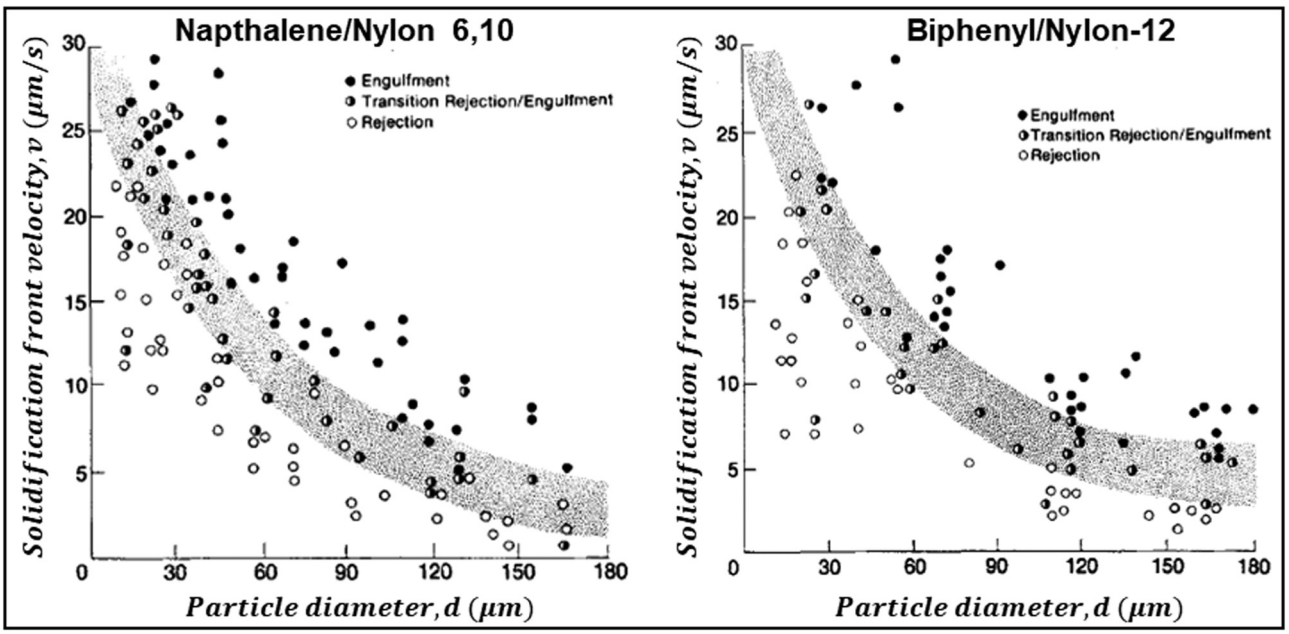

Fig. 2 Data from experiments where dispersions of Nylon particles in naphthalene (left) and biphenyl (right) were frozen. The figures show the solidification front velocity of naphthalene (left) and biphenyl (right) *versus* the diameter of nylon particles. At low interface velocities, the solid–liquid interface is planar and the particles are rejected by the growing front. With an increase in velocity the interface becomes unstable. Above a particle-size dependent critical velocity, the particles are engulfed by the growing front. Reprinted with permission from ref. 79. Copyright (1981) AIP Publishing.

impingement. In recent work, dilute colloidal dispersions were frozen to form isolated colloidal clusters, and the cluster size distribution was analysed to gain insight into the mechanism of their assembly.[35,36] Samples were frozen using one of the two protocols: isotropically, where no temperature gradient was imposed on the sample, or unidirectionally as schematically shown in Fig. 3(a). In both protocols, the cluster size distributions obtained were described by a power law, $P_n \sim n^{-\xi}$, where P_n represents the probability of finding a cluster comprising n particles. For isotropic freezing, experiments and simulations yielded $\xi \approx 2$ over two orders of magnitude in the dispersion concentration (all sufficiently dilute that percolated structures did not form). In contrast, for unidirectional freezing, the exponent ξ decreased with concentration from about 3.5 to $\approx$2 over two decades of particle concentration from 0.001% to 0.1% (Fig. 3(b)). These experimental results are near quantitatively captured by simulations that invoke only the expulsion of the colloids by the growing ice front, neglecting hydrodynamics, inter-particle interactions (except hard sphere contact repulsion) and details of ice growth. Therefore, it is rationalized that the qualitative difference in cluster size distribution in the two freezing protocols arises from how the ice crystals fill space as they grow and impinge. Ice crystals that are nucleated randomly in the bulk of the dispersion grow isotropically to

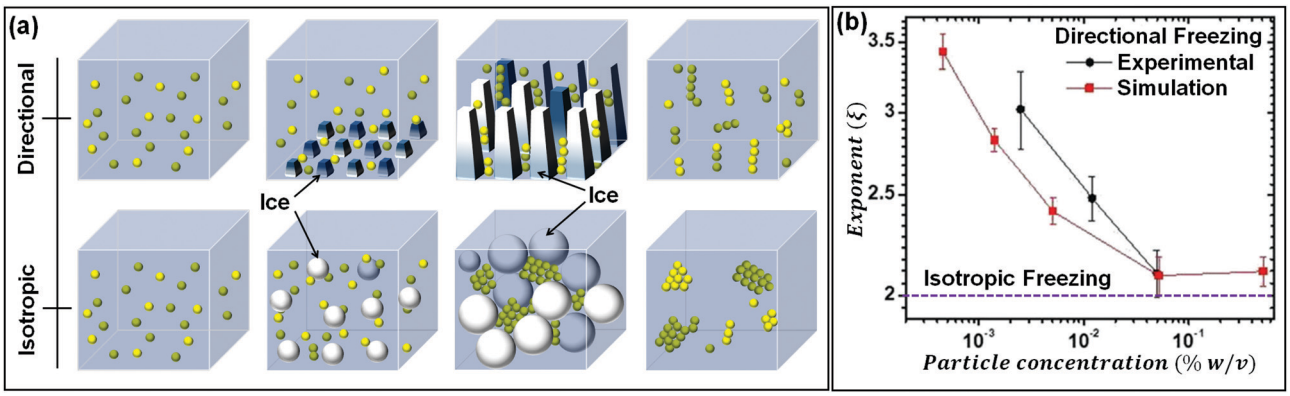

Fig. 3 (a) Schematic representation of the time dependent structural evolution when a dilute dispersion of colloidal particles is frozen unidirectionally (top panel) and under isotropic conditions (bottom panel). Particles are expelled by the growing ice front and are assembled into isolated clusters that reflect the geometry of ice crystal impingement. (b) The size distribution of particle clusters follows a power law for both isotropic and directional freezing. The power law exponent is shown, as a function of particle concentration for directional freezing (solid black – experimental and red line – simulations) and for isotropic freezing (dashed purple line). Adapted with permission from ref. 36. Copyright (2021) Royal Society of Chemistry.

form pockets at late stages that trap particles, all of which must then consolidate into a single cluster. Therefore, the cluster size distribution remains the same, independent of particle concentration. In contrast, for unidirectional ice growth, colloidal particles are trapped in between walls of ice. With time, these walls thicken and grow towards each other, trapping colloidal particles between them. However, since the colloids can diffuse over the surface of the wall, the colloids between two walls do not necessarily assemble to form one cluster. Thus, differences in the cluster size distribution result from differences in the topology of liquid pockets as the ice crystals impinge, and from the distribution of particles in these pockets.

The self-assembly of Brownian colloids expelled at the freezing front depends on their shape, size distribution and inter-particle interactions. Im and Park have demonstrated that freezing dispersions of a monodisperse charge-stabilized polystyrene latex resulted in the formation of three-dimensionally ordered structures, as shown in Fig. 4, that exhibit a photonic band-gap.[97] They reported that rapid freezing resulted in the formation of curved or spherical assemblies (Fig. 4(b) and (c)), while slower freezing rates resulted in planar crystals (Fig. 4(a)) with fewer defects. Expulsion of Brownian monodisperse polystyrene colloids at the ice–water interface in unidirectional freezing has been shown to give rise to colloidal crystals arranged as oriented columnar domains.[99]

Crystallization of charge stabilized colloids expelled at a freezing front is controlled by an interplay between the particle Brownian diffusivity and the rate at which a particle attaches to and detaches from a colloidal crystal (which, in turn, depends on particle concentration and inter-particle interactions). Experiments that examined the systematic variation of the freezing front growth velocity on the ordering of monodisperse colloids have identified that colloidal crystallization is controlled by the Peclet number, $\mathrm{Pe} = dv/D$, where d is the colloidal particle diameter, v is the velocity of the freezing front and $D = k_B T/\zeta$ is the Brownian diffusivity of the colloid at temperature T and in a medium with hydrodynamic resistance ζ.[100] However, we note that this analysis only balances the time scales for Brownian diffusivity ($=d^2/D$) with that for convection ($=d/v$) and does not account for the role of inter-particle interactions. The inadequacy of this approach has been pointed out in the literature upon evaporation of colloidal dispersions.[101] It is known that attractive interactions between colloids inhibit positional reorganization in particle assemblies and preclude the crystallization of even monodisperse colloids.[102] For colloids that interact as hard spheres, equilibrium colloidal crystallization is determined only by the particle volume fraction.[103] Brownian dynamics simulations indicate that for a hard sphere colloidal dispersion that is concentrated by a moving interface (for example, by evaporation or freezing), intermediate values of Pe promote colloidal crystallization.[104] In the low Pe regime, Brownian diffusion dominates and particle crystallization is determined by their concentration, as in the equilibrium case. At high Pe, particles pile up at the freezing front and kinetic constraints on particle reorganization inhibit colloidal crystallization, as observed in the experiments on charge stabilized colloids.[100] Ice templating experiments typically employ charge stabilized colloids. In charge stabilized particles, the strength and range of inter-particle interactions can be tuned by changing the ionic strength or by the addition of non-adsorbing polymers (to induce depletion interactions) or adsorbing polymers (to induce interactions as particles approach each other by charge correlations or bridging). A thorough, systematic investigation of the combined effects of particle size (that determines the Brownian diffusivity), crystallization rate (that could also determine the strength of particle consolidation in the aggregate[105]) and inter-particle interactions on particle ordering is still not available in the literature. When the size polydispersity of colloidal dispersions exceeds about 10%, they cannot crystallize.[106] Ice templating of bidisperse colloidal dispersions comprising micron size particles and nanometer size sols has been used to produce crack-free high density ceramics with hierarchical porosity.[41,107] It was reported that assemblies of micron sized inorganic particles consolidated by ice templating have insufficient strength and require freeze drying to withstand stresses generated by removal of the ice template. In contrast, objects assembled by ice-templating of bidisperse colloidal dispersions could be recovered intact by normal drying. Anisotropic rigid colloidal particles exhibit entropically driven orientational ordering with an increase in concentration, as first analysed by Onsager.[108] Such lyotropic orientational ordering transitions have been experimentally observed in both rod-like and plate-like colloids that interact through hard-sphere or screened Coulombic interactions.[109–112] When a dispersion containing anisotropic colloids is ice-templated, their expulsion from the frozen phase results in an increase in their local concentration such that liquid crystalline phases may form. This has important implications for the structure of the assembled colloids when they are consolidated by impingement of the frozen phase. As a rod-like colloid is approached by a moving front, the resultant hydrodynamic forces lead to particle alignment.[113] For low Pe, the rod aligns with its major axis parallel to the moving front.

When a dispersion of anisotropic particles is subjected to unidirectional freezing, the particles are consolidated into lamellar structures. The majority of this research is focused on bioinspired approaches that try to mimic the structure of various natural materials. Ice templating of dispersions of high

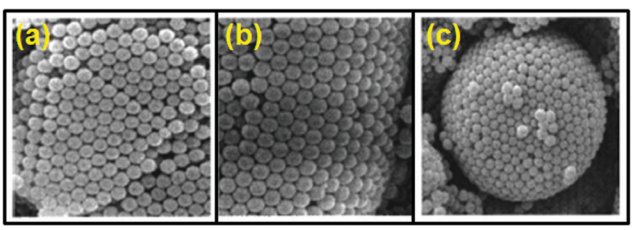

Fig. 4 SEM images of (a) planar, (b) curved, and (c) spherical structures obtained by the self-assembly of size-monodisperse polystyrene latex by freezing aqueous dispersions. Reprinted with permission from ref. 97. Copyright (2002) AIP Publishing.

aspect ratio rod-like or fiber-like structures,[114] especially bio-derived fibers such as chitin, amyloid fibers,[115] cellulose nanofibers,[48,116–119] keratin filaments,[120,121] SiC fibres,[59] platelets,[61,122–127] and nanorods,[128] has been reported. However, there are few investigations that systematically probe the effect of particle shape or colloid aspect ratio on freezing-induced orientational phase transitions. Thus, a comprehensive understanding of orientation development in ice templated rod-like dispersions is lacking in the literature. Depending on the nature of the anisotropy, the crystals can organize anisotropic particles with a specific favoured orientation. For example, for plate-like two dimensional colloidal suspensions, unidirectional freezing is used to produce macroporous materials with aligned platelets in the wall. Here, aligned platelets in the macroporous materials can only be achieved when the ice crystals are large enough compared to the platelet size. Densification, required to attain superior mechanical properties, remains a major challenge for ice-templating of large platelet suspensions. By controlling the anisotropy of the particles, an anisotropic functional response of the material can be achieved at the macro-sample scale. Hexagonal boron nitride anisotropic particles are characterized by different thermal conductivity in in-plane and out-of-plane orientations. Better orientation (and therefore, anisotropic response) can be obtained when samples are prepared using freezing rather than by the use of external electric or magnetic fields.[122] Even if there is no functional anisotropy, the texture of the materials can also be used to improve the mechanical behavior of the materials. In one report, low concentration cellulose nanocrystal dispersions were aligned into a nematic phase in the lamellar space between ice crystals, and were consolidated into an oriented assembly.[129] The same work also investigated higher concentration dispersions that already showed chiral nematic order assembly. When these were subjected to directional freezing, the nematic assemblies were further organized into lamellar structures. In another report cellulose nanofiber and nanocrystal dilute dispersions were shown to form aligned structures upon unidirectional freezing.[128] The authors noted that the alignment of cellulosic structures could be disrupted by changing the ionic strength and/or pH of the original dispersion, thereby introducing attractive inter-colloid interactions. However, they also noted that alignment was not significantly affected for higher initial dispersion concentrations where the cellulose nanostructures gelled. In another report, it was observed that when a hydrogel of chiral cellulose nanocrystals is frozen, the growing ice crystals compress the nanocrystals resulting in a decrease in their helical pitch to generate photonic structures at visible wavelengths.[130] Nematic liquid crystal dispersions of silver nanowires in PVA–water have also been directionally ice templated, and it was reported that the silver nanowires were oriented perpendicular to the freezing direction.[114] Thus, during ice templating the orientation of the particles appears to depend on several factors, including the chemistry of the ice templated materials, their aspect ratio and inter-particle interactions.

There are important implications of particle alignment induced by the growing ice front on the properties of ice templated structures. In recent work,[98] hematite dispersions of colloids with systematically varied aspect ratios (from about 1 to 4) were ice templated to form nanocomposite monoliths. The preparation protocol for ice-templated macroporous scaffolds and the microstructure of the wall comprising hematite particles with varying aspect ratios are shown in Fig. 5(a)–(f), where the hematite particles are held together in a mesh of crosslinked polymers. It was observed that monoliths comprising nearly isotropic particles (aspect ratio ~ 1) showed a linear dependence of their modulus on the nominal density ($E \sim \rho$) as shown in Fig. 5(g). There was no preferred local particle orientation of the anisotropic hematite particles observed, as evident from the SEM micrographs (Fig. 5(d) and (f)). However, for these monoliths, it was observed that $E \sim \rho^{1.4}$ (for aspect ratio $\sim$ 2.2) and $E \sim \rho^2$ (for aspect ratio $\sim$ 4), a qualitatively different dependence (Fig. 5(h) and (i)). Thus, a systematic understanding of how particle anisotropy and interactions govern their packing during ice templating has implications for the control of properties of the resultant monolith. Experiments and DEM simulations have been used to investigate the assembly of plate-like faceted colloids during unidirectional freezing.[122] The particles are expelled by the growing ice and are trapped in the dispersion between the sheet-like ice. When these sheets thicken and move towards each other, particles at the moving interface are reoriented with their axis normal to the interface. As the dispersion concentration continues to increase, the particles closest to the interface become aligned while those away from the interface eventually jam into a state with a lower degree of order. They report that particle alignment is driven largely by contact repulsion and is observed even for particles with relatively low anisotropy. Similar behaviour is observed for unidirectional ice-templating of plate-like alumina colloids dispersed in aqueous chitosan/gelatin[123] as shown in Fig. 6(a). Here, additionally, electrostatic interactions between the cationic chitosan/gelatin and the anionic alumina result in the formation of layered inorganic/polymer composites reminiscent of the structure of nacre as depicted in Fig. 6(b). These observations also suggest that the mechanical properties (Young's modulus, yield strength and toughness) of the ice-templated scaffolds are greatly influenced by the particle shape, size and freezing rate, as described in Fig. 6(c). However, there are also reports on the orientation of plate-like colloids that form interlamellar bridges perpendicular to the moving front in unidirectionally ice templated samples.[131] Local orientational ordering of ice-templated plate like particles is also strongly influenced by interparticle interactions. Ice templating of as-prepared graphene oxide aqueous dispersions results in the random orientational ordering of the graphene oxide sheets. However, ice templating subsequent to the partial reduction of graphene oxide results in highly ordered assemblies with parallel graphene oxide sheets.[57] Such monoliths have been reported to exhibit highly elastic mechanical recovery after large compression and exhibit modulus, $E \sim \rho^2$ (compared with $\sim\rho^3$ for carbon nanoparticles or nanotube foams, with random interparticle orientations).

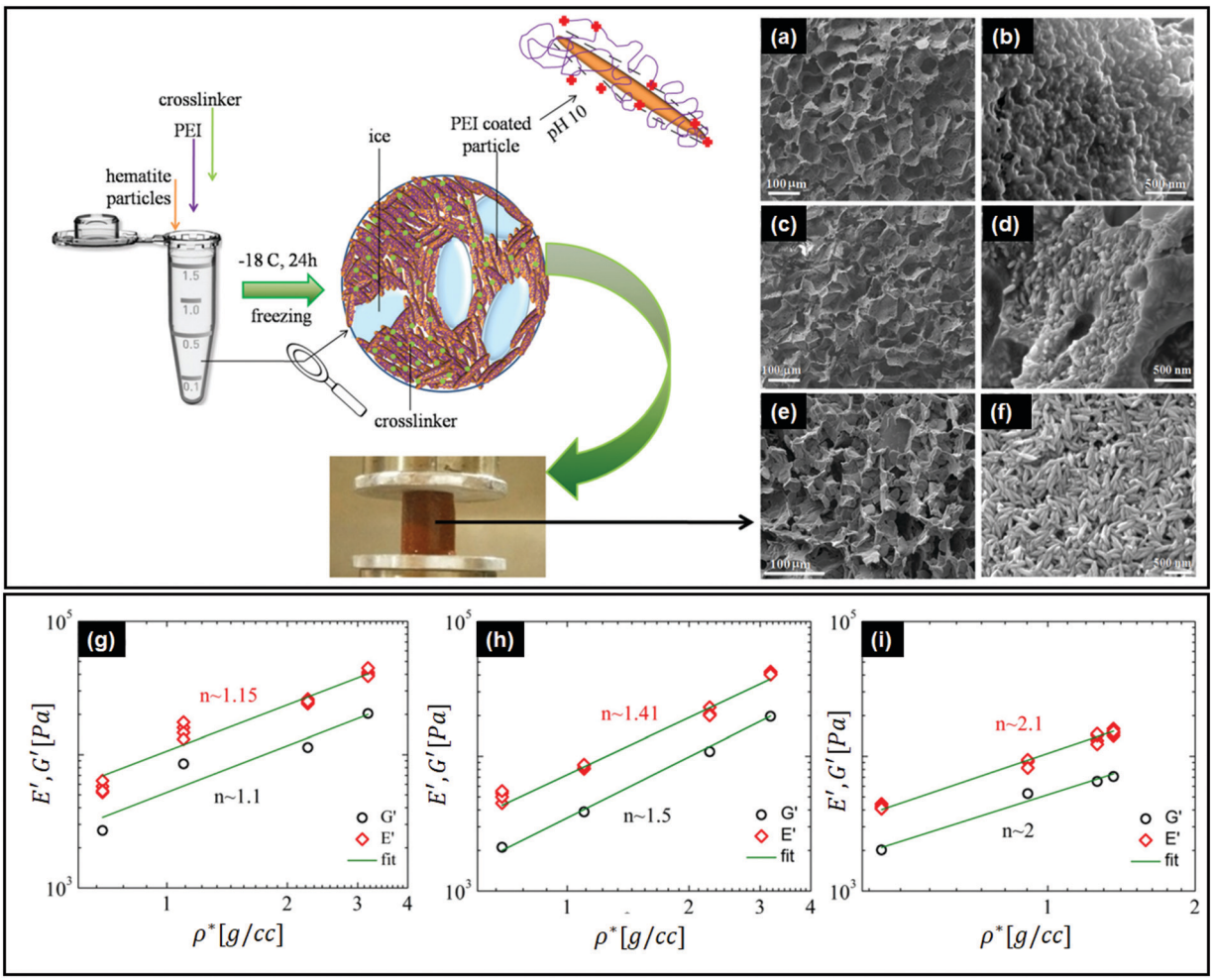

Fig. 5 Top left panel – preparation protocol for ice-templated macroporous scaffolds, comprising walls of hematite particles held together in a mesh of crosslinked polymers. On the right, we observe the SEM micrographs of the walls of the porous monolith made using this protocol. (a and b) Monolith containing hematite particles with aspect ratios of ~1, (c and d) ~2.2 and (e and f) ~4. Bottom panel – mechanical moduli from dynamic experiments in compression (E) and shear (G') modes, as a function of nominal density (ρ^*) for the hematite scaffolds with aspect ratios of (g) ~1, (h) ~2.2, and (i) ~4. Note the systematic change in the power law exponents with the particle aspect ratio. Reprinted with permission from ref. 98. Copyright (2020) AIP Publishing.

When multicomponent dispersions are ice-templated, the composite structure that results is governed by the inter-component interactions and their spatial organization. For example, in ice templated inorganic polymer nanocomposite monoliths, it has been demonstrated that the mechanical properties can be qualitatively different, depending on the processing route.[132] The processing route determines the solvation state of the polymer in the composite, and thereby its ability to participate in crosslinking to mechanically stabilize the monolith. In nacre-mimetic composites, electrostatic interactions between the cationic polymer and anionic plate-like particles in the dispersion provide steric stabilization and result in one-dimensional stacking of alternating inorganic particles and the polymer.[123] Therefore, in this report, the cationic polymer also acts as a dispersant, modifying the colloidal inter-particle interactions. In ice templating, the use of dispersants to stabilize colloids and binders to provide green strength to monoliths is common. These additives, could in addition, also influence the nucleation and growth of ice, and the stability of the frozen state.[133,134] Electrostatic interactions between the components of a dispersion have been exploited to create self-assembled aggregates that are then ice-templated to form monolith structures.[135] The imposition of external fields, such as electric, magnetic and acoustic fields, can influence inter-particle interactions at field strengths lower than that required to affect solvent freezing. This can be used to control particle assembly during ice templating, but is not the focus of this review. The literature on field-induced structural control during ice templating has been reviewed recently.[136]

Finally, we comment on the effect of increasing concentration during freezing on determining the self-assembled structure of amphiphiles. The structure of a dispersed phase is strongly determined by its concentration. When a dispersed phase is expelled at the freezing front, its concentration

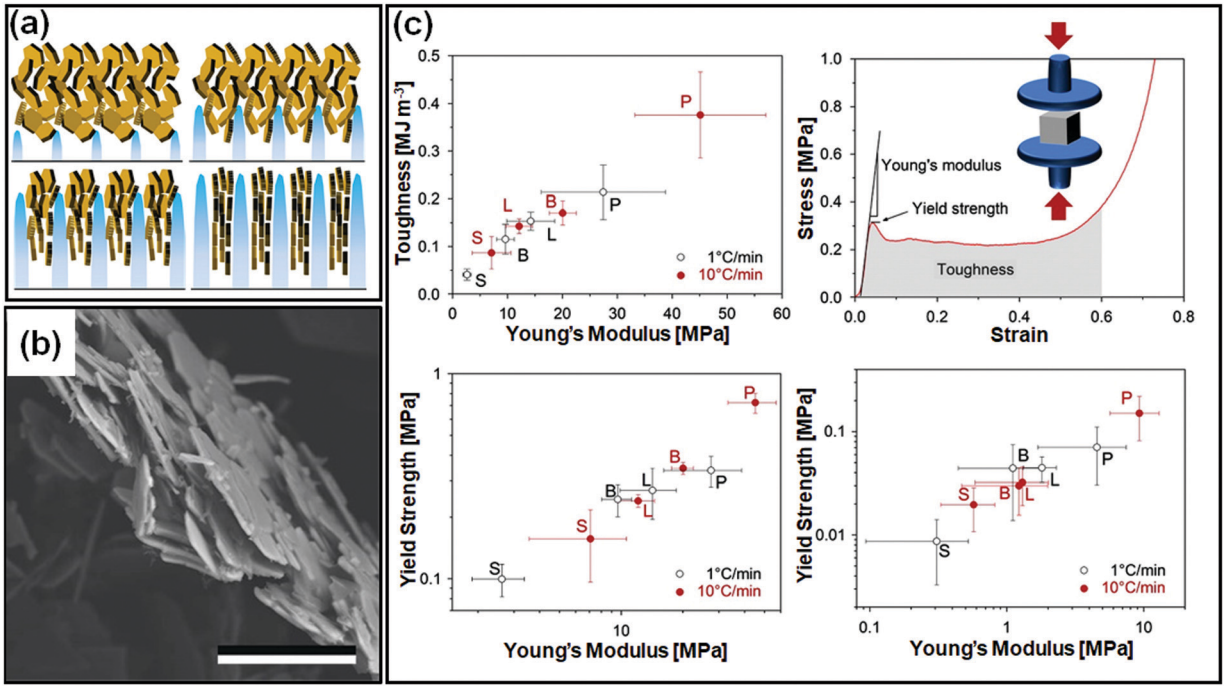

Fig. 6 (a) Unidirectional ice templating of plate-like alumina dispersions in aqueous chitosan/gelatin results in their alignment, as indicated in the schematic. (b) An SEM image of the cross-section of the wall in the macroporous scaffold shows a nacre-like organization with aligned ceramic platelets in a composite structure. (c) Mechanical response of monoliths comprising alumina platelets [P] or isotropic particles with different sizes [S, small and L, large, or B bimodal, comprising S and L particles] prepared at two different freezing rates. The representative stress–strain curve shows that P monoliths exhibit a combination of high toughness and stiffness. Reprinted with permission from ref. 123. Copyright (2013), Elsevier.

increases steadily as freezing proceeds. Close to the impingement of the frozen phase, the dispersed phase concentration is very high, with important consequences for the structure. For example, it has been shown[137] that freezing aqueous solutions of amphiphilic P123 Pluronic copolymers results in the formation of ordered mesophases even when the initial solutions are below their critical micellar temperature (Fig. 7). This results from a continuous increase in the concentration of the amphiphilic copolymer to form dispersed micelles at first, followed by ordered micellar mesophases which was inferred from the time dependent evolution of temperature and concentration and SAXS patterns shown in Fig. 7(a)–(c). This is

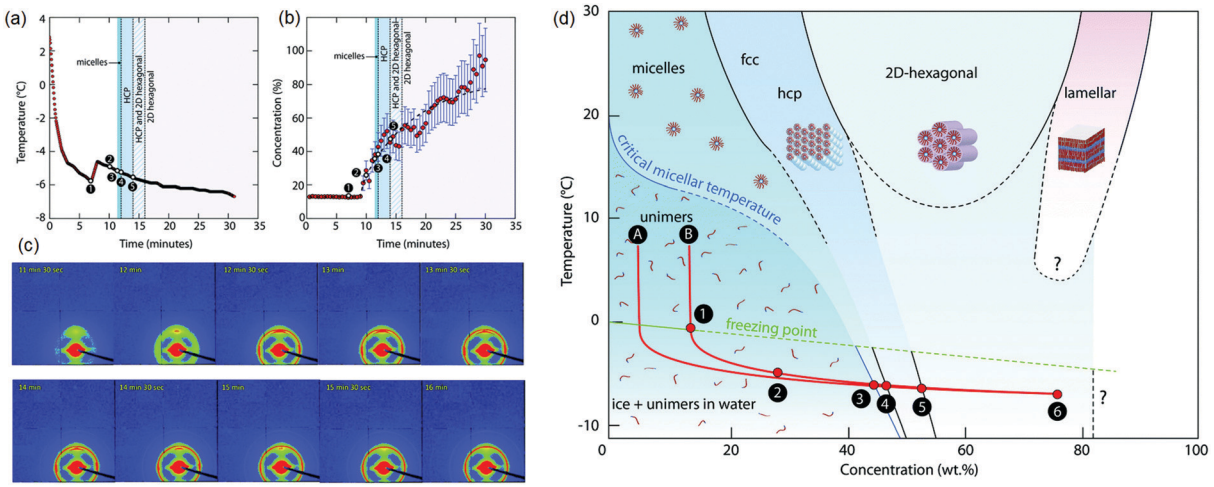

Fig. 7 Freezing induced self-assembly of a 13 wt% aqueous P123 amphiphilic copolymer. Time dependent evolution of (a) temperature and (b) concentration, and (c) SAXS patterns are shown. (d) A concentration–temperature "phase diagram" showing structure formation during freezing-induced self-assembly of aqueous P123. Only P123 unimers are found in solution at first. When ice crystals begin to form (1–2), the concentration of P123 (in the liquid phase) increases, and self-assembled structures are observed (3–4–5). The freezing point (FP) temperature curve and the CMT curve are extrapolated (dashed lines). Reprinted with permission from ref. 137. Copyright (2017), Royal Society of Chemistry.

reminiscent of amphiphilic micellar ordering reported in Evaporation Induced Self-Assembly (EISA) protocols.[138] Using a similar concept, an aqueous dispersion of block copolymer micelles was frozen to form a hexagonal mesophase that was subsequently templated to form mesoporous silica walls in a macroporous ice-templated monolith.[139] Freezing has also been shown to result in structural changes in protein dispersions, for example, the formation of β-sheets in silk fibroin dispersions leading to gelation.[140,141] Other examples in the literature have suggested using ice templating to spatially organize reactants in the walls of a macroporous monolith[142] and subsequently carry out chemical transformations in the walls such as, for example, the synthesis of microporous zeolites.[143] The possibility that the rate of chemical reactions can be modulated due to the confinement or increased reactant concentration during ice templating offers intriguing possibilities. For example, one anticipates that endothermic reactions such as amine-epoxy curing should proceed slowly as the temperature is decreased, through an Arrhenius rate factor. Our group has shown that polyethyleneimine (PEI) reacts with PEG-diepoxide during ice templating, *viz.* at temperatures as low as −18 °C.[64,132] We see no evidence for any substantial progress in the PEI–diepoxide reaction in the initial dilute dispersion at room temperature over the same time period. We reason that the increase in concentration of the reactants as the water freezes more than compensates for the decrease in reaction rate due to cooling. Thus, this reaction is enabled even at low temperatures due to the freezing-induced increase in the reactant concentration. It is possible that such ice-assisted chemistry might be promoted by the existence of a mobile layer on the surface of crystalline ice (first reported by Faraday[144]). The formation of the crosslinked polymer mesh is not limited to the polyethylene imine–diepoxide system and several other chemistries have been demonstrated. For example, Rajamanickam *et al.*[64] have shown that glutaraldehyde can effectively crosslink polyethyleneimine concentrated by freezing to produce self-standing monoliths. Furthermore, they prepared completely biocompatible macroporous monoliths by freezing dispersions of hydroxyapatite particles and gelatin, and by crosslinking gelatin in the frozen state using EDC coupling chemistry. Their group has demonstrated the preparation of monoliths using dispersions of colloidal particles with sizes varying from about 20 nm to several microns; for freezing dispersions in water or DMSO, and for freezing at different cooling rates (by placing in a refrigerator at −18 °C for rapid cooling by plunging in liquid nitrogen). In all these cases, crosslinking of the polymer mesh surrounding the colloidal particles resulted in the formation of monoliths capable of recovering from large compressive strains (nearly 90%). Therefore, the formation of monoliths capable of elastic recovery from compression appears to be governed by the nanocomposite structure produced – rather than the specific nature of the particle, polymer or crosslinker – with mechanical recovery governed by the rubbery crosslinked polymer mesh that surrounds the colloidal particles. Indeed, these monoliths are soft, despite their large inorganic content, pointing to the dominant role of the polymeric mesh in determining the mechanical properties. Therefore, the mechanical properties are highly sensitive to changes in the preparation protocol that affect the formation of the crosslinked polymer mesh. For example, if the frozen sample is lyophilized immediately after freezing, and before the crosslinking reaction proceeds to a substantial extent, then the dilute polymer chains are exposed to air (bad solvent conditions) rather than to water (good solvent). Under these conditions, there is a change in the conformation of the dilute polymer chains as they collapse. Crosslinking these samples at the same temperature and for the same duration as the frozen samples results in the formation of a monolith that is brittle, and that forms cracks even for small compressive strains (of the order of 5%).[132] Thus, the formation of crosslinks to prepare a polymer mesh is less efficient for the case of collapsed polymer chains and produces monoliths with a qualitatively different (brittle) mechanical response. We note that for the case of effective crosslinking, intact centimeter-scale monoliths can be obtained simply by thawing and drying the ice templated samples, obviating the need for lyophilization. Such ice-assisted reactions have broad implications for materials and environmental chemistry and represent an interesting area of research.[145–151]

5 Summary

There have been several recent reviews on materials synthesis using ice templating, attesting to the growing interest in this field. In this review, we focus on the role of solute–freezing front interactions, and particularly on solute–solute interactions, in determining the self-assembled structure that results from ice templating. As ice crystals grow, they expel solute to the liquid regions. The increasing solute concentrations in these regions result in strong solute–solute interactions. Therefore, self-assembled structure formation is governed by a combination of thermodynamic and kinetic factors: the range and strength of solute–solute interactions, and a balance between the rate of growth of the freezing front and solute diffusivity. While literature analyses have considered the influence of the Peclet number (a non-dimensional number that scales the velocity of the moving front with that of solute diffusion), the role of solute–solute interactions has remained underexplored. This represents an important and interesting avenue for exploration. Traditionally, stabilizers and dispersants have been used, based on experience, to keep the solute suspended until the ice crystals impinged. However, as the solute particles are concentrated during freezing, their interactions play a role in determining the structure. For example, strong attractive interactions could result in the formation of a jammed state that could influence the propagation of the freezing front. Alternately, excluded volume interactions determined by the solute shape and size could lead to crystallization or orientational ordering in the walls of ice templated monoliths. A thorough, systematic investigation of the combined effects of particle size and shape (that determine Brownian

diffusivity and excluded volume interactions), crystallization rate (that could also determine the strength of particle consolidation in the aggregate) and inter-particle interactions on particle ordering is still not available in the literature. Understanding these aspects will have importance for the design of ice-templated materials with improved properties, based on appropriate choice of solute in the initial dispersion. A freezing induced increase in the solute concentration can also promote chemical reactions that can be used to create composite monoliths with exquisite control over their mechanical response. It is believed that there exists a thin mobile layer of quasi-liquid water at the ice interface which may drive the reaction even at very low temperatures. The relevance of this layer to ice-templated materials remains to be investigated. What is the importance of this molecular mobility in the progress of chemical reactions under frozen conditions? Can ordered macromolecular structures be prepared under such conditions? There are several such interesting questions that remain unanswered. The aspect of controlling the structures in monolith walls by tailoring solute–solute interactions has attracted relatively less attention in the community. By pointing to the opportunities for materials control through tailored solute–solute interactions, we hope that this aspect will be investigated more thoroughly in the near future.

Conflicts of interest

The authors report no conflicts of interest related to this work.

Acknowledgements

G. K. gratefully acknowledges the start-up funding from IIT-Bombay. R. M. gratefully acknowledges IIT-Bombay for the award of an Institute Postdoctoral Fellowship.

References

1 G. M. Whitesides and B. Grzybowski, *Science*, 2002, **295**, 2418–2421.
2 P. Jiang, J. Bertone, K. S. Hwang and V. Colvin, *Chem. Mater.*, 1999, **11**, 2132–2140.
3 C. Murray, C. Kagan and M. Bawendi, *Science*, 1995, **270**, 1335–1338.
4 Y. Mino, S. Watanabe and M. T. Miyahara, *ACS Appl. Mater. Interfaces*, 2012, **4**, 3184–3190.
5 M. Janjua, S. Nudurupati, P. Singh and N. Aubry, *Electrophoresis*, 2011, **32**, 518–526.
6 A. B. Subramaniam, M. Abkarian and H. A. Stone, *Nat. Mater.*, 2005, **4**, 553–556.
7 Y. Lin, H. Skaff, T. Emrick, A. Dinsmore and T. P. Russell, *Science*, 2003, **299**, 226–229.
8 J. Huang, F. Kim, A. R. Tao, S. Connor and P. Yang, *Nat. Mater.*, 2005, **4**, 896–900.
9 E. Rabani, D. R. Reichman, P. L. Geissler and L. E. Brus, *Nature*, 2003, **426**, 271–274.
10 Z. Li and Z. Lin, *Polym. Int.*, 2021, DOI: 10.1002/pi.6327.
11 Z. Li, J. Peng and Z. Lin, *Giant*, 2021, **5**, 100048.
12 S. Deville, *Adv. Eng. Mater.*, 2008, **10**, 155–169.
13 A. G. Slater and A. I. Cooper, *Science*, 2015, **348**, aaa8075.
14 A. Stein, S. G. Rudisill and N. D. Petkovich, *Chem. Mater.*, 2014, **26**, 259–276.
15 S. Deville, *Freezing colloids: observations, principles, control, and use*, Springer International Publishing, 2017.
16 R. F. Lobo, S. I. Zones and M. E. Davis, *J. Inclusion Phenom. Mol. Recognit. Chem.*, 1995, **21**, 47–78.
17 C. Kresge, M. Leonowicz, W. J. Roth, J. Vartuli and J. Beck, *Nature*, 1992, **359**, 710–712.
18 A. Barbetta, G. Rizzitelli, R. Bedini, R. Pecci and M. Dentini, *Soft Matter*, 2010, **6**, 1785–1792.
19 A. C. Pierre and G. M. Pajonk, *Chem. Rev.*, 2002, **102**, 4243–4266.
20 O. D. Velev and E. W. Kaler, *Adv. Mater.*, 2000, **12**, 531–534.
21 K. H. Rhodes, S. A. Davis, F. Caruso, B. Zhang and S. Mann, *Chem. Mater.*, 2000, **12**, 2832–2834.
22 A. Stein, F. Li and N. R. Denny, *Chem. Mater.*, 2008, **20**, 649–666.
23 R. A. Caruso and M. Antonietti, *Chem. Mater.*, 2001, **13**, 3272–3282.
24 M. Breulmann, S. Davis, S. Mann, H.-P. Hentze and M. Antonietti, *Adv. Mater.*, 2000, **12**, 502–507.
25 Y. Zhang, S. Zha and M. Liu, *Adv. Mater.*, 2005, **17**, 487–491.
26 S. A. Davis, H. M. Patel, E. L. Mayes, N. H. Mendelson, G. Franco and S. Mann, *Chem. Mater.*, 1998, **10**, 2516–2524.
27 A. Böker, Y. Lin, K. Chiapperini, R. Horowitz, M. Thompson, V. Carreon, T. Xu, C. Abetz, H. Skaff and A. Dinsmore, *et al.*, *Nat. Mater.*, 2004, **3**, 302–306.
28 Y. Sakatani, C. Boissière, D. Grosso, L. Nicole, G. J. Soler-Illia and C. Sanchez, *Chem. Mater.*, 2008, **20**, 1049–1056.
29 D. Walsh, L. Arcelli, T. Ikoma, J. Tanaka and S. Mann, *Nat. Mater.*, 2003, **2**, 386–390.
30 E. M. Herzig, K. White, A. B. Schofield, W. C. Poon and P. S. Clegg, *Nat. Mater.*, 2007, **6**, 966–971.
31 V. Anderson, E. Terentjev, S. Meeker, J. Crain and W. Poon, *Eur. Phys. J. E: Soft Matter Biol. Phys.*, 2001, **4**, 11–20.
32 K. P. Sharma, A. K. Ganai, S. S. Gupta and G. Kumaraswamy, *Chem. Mater.*, 2011, **23**, 1448–1455.
33 H. Zhang and A. I. Cooper, *Soft Matter*, 2005, **1**, 107–113.
34 X. Shen, L. Chen, D. Li, L. Zhu, H. Wang, C. Liu, Y. Wang, Q. Xiong and H. Chen, *ACS Nano*, 2011, **5**, 8426–8433.
35 G. Kumaraswamy, B. Biswas and C. K. Choudhury, *Faraday Discuss.*, 2016, **186**, 61–76.
36 B. Biswas, M. Misra, A. S. Bisht, S. K. Kumar and G. Kumaraswamy, *Soft Matter*, 2021, **17**, 4098–4108.
37 G. Ma, Z. Wang, J. Chen, R. Yin, B. Chen and J. Nie, *New J. Chem.*, 2014, **38**, 1211–1217.
38 B. S. Kim, M. K. Lee and J. Lee, *Macromol. Res.*, 2013, **21**, 194–201.
39 A. Gondolini, E. Mercadelli, S. Casadio and A. Sanson, *J. Eur. Ceram. Soc.*, 2022, **42**, 1053–1060.
40 X. Y. Liu, J. M. Yang, L. S. Zha and Z. J. Jiang, *Chin. J. Polym. Sci.*, 2014, **32**, 1544–1549.

41 J. Laurie, C. Bagnall, B. Harris, R. Jones, R. Cooke, R. Russell-Floyd, T. Wang and F. Hammett, *J. Non-Cryst. Solids*, 1992, **147**, 320–325.
42 H. Zhang, D. Edgar, P. Murray, A. Rak-Raszewska, L. Glennon-Alty and A. I. Cooper, *Adv. Funct. Mater.*, 2008, **18**, 222–228.
43 X. Zeng, L. Ye, S. Yu, R. Sun, J. Xu and C.-P. Wong, *Chem. Mater.*, 2015, **27**, 5849–5855.
44 Y. Si, X. Wang, L. Dou, J. Yu and B. Ding, *Sci. Adv.*, 2018, **4**, eaas8925.
45 B. H. Yoon, E. J. Lee, H. E. Kim and Y. H. Koh, *J. Am. Ceram. Soc.*, 2007, **90**, 1753–1759.
46 M. Barrow, A. Eltmimi, A. Ahmed, P. Myers and H. Zhang, *J. Mater. Chem.*, 2012, **22**, 11615–11620.
47 X. Wu, Y. Liu, X. Li, P. Wen, Y. Zhang, Y. Long, X. Wang, Y. Guo, F. Xing and J. Gao, *Acta Biomater.*, 2010, **6**, 1167–1177.
48 J. Lee and Y. Deng, *Soft Matter*, 2011, **7**, 6034–6040.
49 M. J. Hortiguela, I. Aranaz, M. C. Gutierrez, M. L. Ferrer and F. del Monte, *Biomacromolecules*, 2011, **12**, 179–186.
50 J. W. Kim, K. Taki, S. Nagamine and M. Ohshima, *Langmuir*, 2009, **25**, 5304–5312.
51 P. Song, H. Qin, H.-L. Gao, H.-P. Cong and S.-H. Yu, *Nat. Commun.*, 2018, **9**, 1–9.
52 H. L. Gao, L. Xu, F. Long, Z. Pan, Y. X. Du, Y. Lu, J. Ge and S. H. Yu, *Angew. Chem.*, 2014, **126**, 4649–4654.
53 A. Knoìller, S. Kilper, A. M. Diem, M. Widenmeyer, T. Runcìevski, R. E. Dinnebier, J. Bill and Z. Burghard, *Nano Lett.*, 2018, **18**, 2519–2524.
54 M. C. Gutierrez, M. J. Hortigüela, J. M. Amarilla, R. Jiménez, M. L. Ferrer and F. Del Monte, *J. Phys. Chem. C*, 2007, **111**, 5557–5560.
55 S. Nardecchia, M. C. Serrano, M. C. Gutiérrez, M. T. Portolés, M. L. Ferrer and F. del Monte, *Adv. Funct. Mater.*, 2012, **22**, 4411–4420.
56 J. L. Vickery, A. J. Patil and S. Mann, *Adv. Mater.*, 2009, **21**, 2180–2184.
57 L. Qiu, J. Z. Liu, S. L. Chang, Y. Wu and D. Li, *Nat. Commun.*, 2012, **3**, 1–7.
58 H. Zhang, I. Hussain, M. Brust, M. F. Butler, S. P. Rannard and A. I. Cooper, *Nat. Mater.*, 2005, **4**, 787–793.
59 C. Ferraro, E. Garcia-Tuñon, V. G. Rocha, S. Barg, M. D. Fariñas, T. E. G. Alvarez-Arenas, G. Sernicola, F. Giuliani and E. Saiz, *Adv. Funct. Mater.*, 2016, **26**, 1636–1645.
60 S. Deville, E. Saiz, R. K. Nalla and A. P. Tomsia, *Science*, 2006, **311**, 515–518.
61 F. Bouville, E. Maire, S. Meille, B. Van de Moortèle, A. J. Stevenson and S. Deville, *Nat. Mater.*, 2014, **13**, 508–514.
62 Q. Cheng and L. Jiang, *Angew. Chem., Int. Ed.*, 2017, **56**, 934–935.
63 A. Wat, J. I. Lee, C. W. Ryu, B. Gludovatz, J. Kim, A. P. Tomsia, T. Ishikawa, J. Schmitz, A. Meyer and M. Alfreider, *et al.*, *Nat. Commun.*, 2019, **10**, 1–12.
64 R. Rajamanickam, S. Kumari, D. Kumar, S. Ghosh, J. C. Kim, G. Tae, S. Sen Gupta and G. Kumaraswamy, *Chem. Mater.*, 2014, **26**, 5161–5168.
65 S. Chatterjee, K. Shanmuganathan and G. Kumaraswamy, *ACS Appl. Mater. Interfaces*, 2017, **9**, 44864–44872.
66 J. Wang, Z. Xu, J. C. Eloi, M. M. Titirici and S. J. Eichhorn, *Adv. Funct. Mater.*, 2022, 2110862.
67 A. Vu, Y. Qian and A. Stein, *Adv. Energy Mater.*, 2012, **2**, 1056–1085.
68 G. Li, Z. Liu, Q. Huang, Y. Gao, M. Regula, D. Wang, L. Q. Chen and D. Wang, *Nat. Energy*, 2018, **3**, 1076–1083.
69 S. Li, G. Tian, R. Xiong, R. He, S. Chen, H. Zhou, Y. Wu, Z. Han, C. Yu and S. Cheng, *et al.*, *Energy Storage Mater.*, 2022, **46**, 443–451.
70 C. Huang and P. S. Grant, *J. Mater. Chem. A*, 2018, **6**, 14689–14699.
71 K. Qin, C. Parisi and F. M. Fernandes, *J. Mater. Chem. B*, 2021, **9**, 889–907.
72 S. Deville, *Scr. Mater.*, 2018, **147**, 119–124.
73 K. L. Scotti and D. C. Dunand, *Prog. Mater. Sci.*, 2018, **94**, 243–305.
74 G. Shao, D. A. Hanaor, X. Shen and A. Gurlo, *Adv. Mater.*, 2020, **32**, 1907176.
75 I. Nelson and S. E. Naleway, *J. Mater. Res. Technol.*, 2019, **8**, 2372–2385.
76 J. Yang, W. Yang, W. Chen and X. Tao, *Prog. Polym. Sci.*, 2020, **109**, 101289.
77 H. Joukhdar, A. Seifert, T. Jüngst, J. Groll, M. S. Lord and J. Rnjak-Kovacina, *Adv. Mater.*, 2021, **33**, 2100091.
78 J. X. Yap, C. Leo, N. H. Mohd Yasin, P. L. Show, D. T. Chu, V. Singh and C. Derek, *Bioengineered*, 2022, **13**, 2226–2247.
79 S. Omenyi, A. Neumann, W. Martin, G. Lespinard and R. Smith, *J. Appl. Phys.*, 1981, **52**, 796–802.
80 M. I. Gibson, *Polym. Chem.*, 2010, **1**, 1141–1152.
81 S. Auer and D. Frenkel, *Nature*, 2001, **409**, 1020–1023.
82 H. Tetik, D. Feng, S. W. Oxandale, G. Yang, K. Zhao, K. Feist, N. Shah, Y. Liao, Z. C. Leseman and D. Lin, *ACS Appl. Mater. Interfaces*, 2021, **13**, 924–931.
83 N. Zhao, M. Li, H. Gong and H. Bai, *Sci. Adv.*, 2020, **6**, eabb4712.
84 H. Bai, Y. Chen, B. Delattre, A. P. Tomsia and R. O. Ritchie, *Sci. Adv.*, 2015, **1**, e1500849.
85 L. Fan, J. L. Li, Z. Cai and X. Wang, *ACS Nano*, 2018, **12**, 5780–5790.
86 H. Niinomi, T. Yamazaki, H. Nada, T. Hama, A. Kouchi, J. T. Okada, J. Nozawa, S. Uda and Y. Kimura, *J. Phys. Chem. Lett.*, 2020, **11**, 6779–6784.
87 J. Dash, A. Rempel and J. Wettlaufer, *Rev. Mod. Phys.*, 2006, **78**, 695.
88 Y. Nagata, T. Hama, E. H. Backus, M. Mezger, D. Bonn, M. Bonn and G. Sazaki, *Acc. Chem. Res.*, 2019, **52**, 1006–1015.
89 B. Slater and A. Michaelides, *Nat. Rev. Chem.*, 2019, **3**, 172–188.
90 K. Murata, H. Asakawa, K. Nagashima, Y. Furukawa and G. Sazaki, *Proc. Natl. Acad. Sci. U. S. A.*, 2016, **113**, E6741–E6748.
91 J. Rutter and B. Chalmers, *Can. J. Phys.*, 1953, **31**, 15–39.
92 H. Keith and F. Padden Jr, *J. Appl. Phys.*, 1963, **34**, 2409–2421.

93 W. W. Mullins and R. Sekerka, *J. Appl. Phys.*, 1964, **35**, 444–451.
94 S. Peppin, J. Wettlaufer and M. Worster, *Phys. Rev. Lett.*, 2008, **100**, 238301.
95 S. Tyagi, C. Monteux and S. Deville, *Sci. Rep.*, 2021, **11**, 1–14.
96 S. Deville, E. Maire, G. Bernard-Granger, A. Lasalle, A. Bogner, C. Gauthier, J. Leloup and C. Guizard, *Nat. Mater.*, 2009, **8**, 966–972.
97 S. H. Im and O. O. Park, *Appl. Phys. Lett.*, 2002, **80**, 4133–4135.
98 G. Kumaraswamy, K. Suresh, H. Lama, M. G. Basavaraj and D. K. Satapathy, *J. Appl. Phys.*, 2020, **128**, 034702.
99 Y. Suzuki, G. Sazaki, K. Hashimoto, T. Fujiwara and Y. Furukawa, *J. Cryst. Grow.*, 2013, **383**, 67–71.
100 J. You, J. Wang, L. Wang, Z. Wang, Z. Wang, J. Li and X. Lin, *Colloids Surf., A*, 2017, **531**, 93–98.
101 A. Lesaine, D. Bonamy, C. L. Rountree, G. Gauthier, M. Impéror-Clerc and V. Lazarus, *Soft Matter*, 2021, **17**, 1589–1600.
102 G. Kumaraswamy, A. M. Dibaj and F. Caruso, *Langmuir*, 2002, **18**, 4150–4154.
103 P. N. Pusey and W. Van Megen, *Nature*, 1986, **320**, 340–342.
104 M. Wang and J. F. Brady, *Soft Matter*, 2017, **13**, 8156–8170.
105 J. Lee and Y. Cheng, *J. Controlled Release*, 2006, **111**, 185–192.
106 P. Pusey, *J. Phys.*, 1987, **48**, 709–712.
107 J. Zheng, D. Salamon, L. Lefferts, M. Wessling and L. Winnubst, *Microporous Mesoporous Mater.*, 2010, **134**, 216–219.
108 L. Onsager, *Ann. N. Y. Acad. Sci.*, 1949, **51**, 627–659.
109 A. Mourchid, A. Delville, J. Lambard, E. Lecolier and P. Levitz, *Langmuir*, 1995, **11**, 1942–1950.
110 H. Lekkerkerker and G. Vroege, *Philos. Trans. R. Soc., A*, 2013, **371**, 20120263.
111 Z. Dogic and S. Fraden, *Curr. Opin. Colloid Interface Sci.*, 2006, **11**, 47–55.
112 Y. Xu, A. Atrens and J. R. Stokes, *Adv. Colloid Interface Sci.*, 2020, **275**, 102076.
113 K. P. Sharma, A. K. Ganai, D. Sen, B. Prasad and G. Kumaraswamy, *J. Phys. Chem. B*, 2013, **117**, 12661–12668.
114 H. E. Romeo, C. E. Hoppe, M. A. Lopez-Quintela, R. J. Williams, Y. Minaberry and M. Jobbágy, *J. Mater. Chem.*, 2012, **22**, 9195–9201.
115 G. Nystroìm, W.-K. Fong and R. Mezzenga, *Biomacromolecules*, 2017, **18**, 2858–2865.
116 L. Liu, L. Bai, A. Tripathi, J. Yu, Z. Wang, M. Borghei, Y. Fan and O. J. Rojas, *ACS Nano*, 2019, **13**, 2927–2935.
117 F. Ram, B. Biswas, A. Torris, G. Kumaraswamy and K. Shanmuganathan, *Cellulose*, 2021, 1–15.
118 F. Martoa, T. Cochereau, P. J. Dumont, L. Orgéas, M. Terrien and M. Belgacem, *Mater. Des.*, 2016, **104**, 376–391.
119 C. Darpentigny, S. Molina-Boisseau, G. Nonglaton, J. Bras and B. Jean, *Cellulose*, 2020, **27**, 233–247.
120 Z. Zhao, H. M. Chua, B. H. R. Goh, H. Y. Lai, S. J. Tan, Z. K. Moay, M. I. Setyawati and K. W. Ng, *J. Biomed. Mater. Res., Part A*, 2022, **110**, 92–104.
121 Z. Zhao, Z. K. Moay, H. Y. Lai, B. H. R. Goh, H. M. Chua, M. I. Setyawati and K. W. Ng, *Macromol. Biosci.*, 2021, **21**, 2000314.
122 F. Bouville, E. Maire and S. Deville, *Langmuir*, 2014, **30**, 8656–8663.
123 P. M. Hunger, A. E. Donius and U. G. Wegst, *J. Mech. Behav. Biomed. Mater.*, 2013, **19**, 87–93.
124 F. Bouville, E. Maire and S. Deville, *J. Mater. Res.*, 2014, **29**, 175–181.
125 F. Bouville, E. Portuguez, Y. Chang, G. L. Messing, A. J. Stevenson, E. Maire, L. Courtois and S. Deville, *J. Am. Ceram. Soc.*, 2014, **97**, 1736–1742.
126 D. Ghosh, M. Banda, S. Akurati, H. Kang and V. O. Fakharizadeh, *Scr. Mater.*, 2017, **138**, 139–144.
127 S. Sabat, S. Sikder, S. K. Behera and A. Paul, *Ceram. Int.*, 2022, **48**, 2893–2897.
128 P. Munier, K. Gordeyeva, L. Bergstroìm and A. B. Fall, *Biomacromolecules*, 2016, **17**, 1875–1881.
129 G. Chu, D. Qu, E. Zussman and Y. Xu, *Chem. Mater.*, 2017, **29**, 3980–3988.
130 Y. Cao, L. Lewis, W. Y. Hamad and M. J. MacLachlan, *Adv. Mater.*, 2019, **31**, 1808186.
131 D. Ghosh, M. Banda, H. Kang and N. Dhavale, *Scr. Mater.*, 2016, **125**, 29–33.
132 K. Suresh, A. Chowdhury, S. K. Kumar and G. Kumaraswamy, *Macromolecules*, 2019, **52**, 5955–5962.
133 J. You, J. Wang, L. Wang, Z. Wang, J. Li, X. Lin and Y. Zhu, *Langmuir*, 2019, **35**, 10446–10452.
134 C. Pekor and I. Nettleship, *Ceram. Int.*, 2014, **40**, 9171–9177.
135 X. Yao, H. Yao and Y. Li, *J. Mater. Chem.*, 2009, **19**, 6516–6520.
136 P. Niksiar, F. Y. Su, M. B. Frank, T. A. Ogden, S. E. Naleway, M. A. Meyers, J. McKittrick and M. M. Porter, *Ceramics*, 2019, **2**, 208–234.
137 P. Albouy, S. Deville, A. Fulkar, K. Hakouk, M. Impéror-Clerc, M. Klotz, Q. Liu, M. Marcellini and J. Perez, *Soft Matter*, 2017, **13**, 1759–1763.
138 C. J. Brinker, Y. Lu, A. Sellinger and H. Fan, *Adv. Mater.*, 1999, **11**, 579–585.
139 J. Dhainaut, G. Piana, S. Deville, C. Guizard and M. Klotz, *Chem. Commun.*, 2014, **50**, 12572–12574.
140 F. Ak, Z. Oztoprak, I. Karakutuk and O. Okay, *Biomacromolecules*, 2013, **14**, 719–727.
141 X. Li, S. Yan, J. Qu, M. Li, D. Ye, R. You, Q. Zhang and D. Wang, *Int. J. Biol. Macromol.*, 2018, **117**, 691–695.
142 J. Dhainaut, S. Deville, I. Amirouche and M. Klotz, *Inorganics*, 2016, **4**, 6.
143 H. Mori, K. Aotani, N. Sano and H. Tamon, *J. Mater. Chem.*, 2011, **21**, 5677–5681.
144 M. Faraday, *London, Edinburgh Dublin Philos. Mag. J. Sci.*, 1859, **17**, 162–169.
145 Z. Tan, X. Guo, Y. Yin, B. Wang, Q. Bai, X. Li, J. Liu and G. Jiang, *Environ. Sci. Technol.*, 2019, **53**, 13802–13811.

146 N. Takenaka, A. Ueda, T. Daimon, H. Bandow, T. Dohmaru and Y. Maeda, *J. Phys. Chem.*, 1996, **100**, 13874–13884.
147 K. Kitada, Y. Suda and N. Takenaka, *J. Phys. Chem. A*, 2017, **121**, 5383–5388.
148 S. M. Agten, D. P. Suylen and T. M. Hackeng, *Bioconjugate Chem.*, 2016, **27**, 42–46.
149 J. Erlandsson, T. Pettersson, T. Ingverud, H. Granberg, P. A. Larsson, M. Malkoch and L. Wågberg, *J. Mater. Chem. A*, 2018, **6**, 19371–19380.
150 R. O. Concubhair and J. R. Sodeau, *Acc. Chem. Res.*, 2013, **46**, 2716–2724.
151 K. Kim and M. J. Park, *Nanoscale*, 2020, **12**, 14320–14338.